Supporting Information

Mochol et al. 10.1073/pnas.1410509112

SI Methods

Surgery and Recording Techniques. Adult, male Sprague–Dawley rats (250–400 g) were anesthetized with urethane (1.5 g/kg), and supplemental doses of 0.15 g/kg were given when necessary after several hours since the initial dose. We also used doses of ketamine (15–25 mg/kg) before the surgery to induce the anesthetized state quickly. Because the time elapsed from the last dose to the beginning of the recordings was at least 3 h and ketamine has a short-lasting effect, the recordings were mostly done under the effect of urethane. Animals were held with a custom-made nasoorbital restraint that left the ears free and uncovered. We removed the left temporal muscle, and a small craniotomy was made over the left primary auditory cortex (A1) and the dura was removed. The location of the recording sites was estimated to be A1 by stereotaxic coordinates and vascular structure (1–3). Next, 32 or 64 channels silicon microelectrodes (Neuronexus Technologies) were slowly inserted into deep layers of the cortex (depth, 600–1,200 μm; lowering speed, ∼1 mm/h). Probes had either eight shanks each with eight staggered recording sites per shank (model Buzsaki 64-A64), or four shanks with two tetrode configurations in each (model A4X2-tet-5mm-150-200-312-A32). Shank spacing was 200 μm in both cases. After establishing a stable recording site, the craniotomy site was covered with 1% agar/artificial cerebrospinal fluid to protect cortex and to stabilize recordings. In three of the experiments, we recorded at several depths (3, 4), but only one depth per animal was included for further analysis. Neuronal signals were high-pass filtered (1 Hz) and amplified (1,000×) using a 64-channel amplifier (Sensorium), recorded at 20-kHz sampling rate with 16-bit resolution using a PC-based data acquisition system (United Electronic Industries) and custom-written software (Matlab Data Acquisition Toolbox; MathWorks) and stored on disk for further analysis.

Acoustic Stimuli. Recordings took place in a single-walled sound isolation chamber (IAC) with sounds presented free field (RP2/ES1; Tucker-Davis). Sound level calibration was performed before each recording session with an ACO-7012 microphone. The microphone was placed facing the speaker at the same distance that the animal's right ear. Acoustic stimuli consisted of single or double clicks (5-ms square pulses; 70 or 75 dB sound pressure level; 50- or 100-ms interclick interval; 2.5- or 3.5-s separation between stimuli). In the present study, we analyzed only the responses to single click.

Datasets Description. We analyzed data from six experimental sessions ($n = 6$ rats). The shortest session lasted 2,892 s, and the longest, 16,347 s (mean + SD, 7,116 ± 4,935). Spike detection and sorting was made off-line, using open-source, semiautomatic clustering methods. The detection and initial clustering was done using Klustakwik (klustakwik.sourceforge.net) (4) or EToS (etos.sourceforge.net) (5, 6). The manual part of clustering was done using Klusters (klusters.sourceforge.net/) (7). The local field potential (LFP) signal was obtained by digitally low-pass filtering (1.25 kHz) the broadband signal from each recording channel. We obtained on average 86 ± 38 (mean + SD; range, 44–147) well-isolated single units and 45 ± 40 (mean + SD; range, 3–103) multiunit spike trains. Both types of spike trains were obtained from waveforms forming a well-separated cluster in principal component analysis space (7), but multiunit spike trains did not show a clear refractory period in the autocorrelogram, indicating that they contained spikes from more than one cell. We analyzed only units that were active through the entire experimental session. We did not impose, however, a constraint on the stationarity of the firing rate because changes in brain state were sometimes accompanied by changes in neuronal firing rate (8) (Fig. S2).

Silence and High Activity Density During Spontaneous and Evoked Activity. We start by defining the spike count $n_i(t;T)$ as the number of spikes fired by the ith single unit in the interval $(t - T/2, t + T/2)$ and the spike count $n_i^{MUA}(t;T)$ as the number of spikes fired by the ith multiunit.

The rate of the pooled population activity (merged activity of single units and multiunits) was defined as follows:

$$r_{pool}(t) = \frac{\sum_{i=1}^{N} n_i(t;\Delta t) + \sum_{i=1}^{N_{MUA}} n_i^{MUA}(t;\Delta t)}{\Delta t}, \qquad \textbf{[S1]}$$

that is, the rate of spikes from all single units and multiunits discretized in bins of size Δt [multiunit spike trains were exclusively used throughout the analysis to compute $r_{pool}(t)$]. The variable $y(t)$ identifying silent bins (i.e., bins with no spikes, Fig. 1*A*, brackets above raster plots), was defined as follows:

$$y(t) = \left\{ \begin{array}{ll} 1, & \text{if } r_{pool}(t) = 0 \\ 0, & \text{otherwise} \end{array} \right\}. \qquad \textbf{[S2]}$$

To characterize the variations in brain state, we divided each recording session into 50-s epochs and quantified the state in each epoch via the silence density. We chose 50 s as a compromise between having a sufficiently large window containing enough activity to give a good estimate of the state and having a sufficiently small window to capture variations in brain state. In each epoch, the silence density (S) during spontaneous activity was defined as the probability that pooled population activity had no spikes. This probability was estimated by computing the average of $y(t)$ evaluated during the periods of spontaneous activity preceding the stimuli presented during the given epoch:

$$S = \langle y(t_k) \rangle_{k \in Spon}, \qquad \textbf{[S3]}$$

where the times $\{t_k\}_{k \in Spon}$ correspond to the center of the kth bin of size Δt within the 1.5 s preceding the stimulus onset times t_{stim}^l:

$$\{t_k\}_{k \in Spon} = \left\{ t_{stim}^l - \frac{\Delta t}{2}, t_{stim}^l - \frac{3\Delta t}{2}, \ldots, t_{stim}^l - \Delta t\left(K - \frac{1}{2}\right);\ l = 1, 2, \ldots, L_{1+2} \right\}, \qquad \textbf{[S4]}$$

where L is a number of stimuli presentation during a given epoch (both single- and double-click presentations were considered, which gave L ranged from 14 to 20 depending on the interstimulus interval) and K is a number of bins of size Δt within the 1.5 s.

With this notation, the average in Eq. **S3** can be written as follows:

$$S = \langle y(t_k) \rangle_{k \in Spon} = \frac{1}{L\,K} \sum_{l=1}^{L} \sum_{k=1}^{K} y\left(t_{stim}^l - \left(k - \frac{1}{2}\right)\Delta t\right). \qquad \textbf{[S5]}$$

The values of S strongly depended on the size of used bin Δt. Small bins (e.g., $\Delta t \sim 1$ ms) led to values of S close to 1 in all epochs (Fig. S1*A*, brown and red curves). Longer bins (e.g., $\Delta t > 640$ ms) gave S values equal or close to zero for all epochs (Fig. S1*A*, dark blue

curves). In both cases, the range of S across epochs was small. S values also depend on the pooled population rate averaged over spontaneous intervals in the epoch $r_{pool} = \langle r_{pool}\{t_k\}\rangle_{k\in Spon}$. A low pooled rate would produce sparse population activity and as a result increase the probability of obtaining silent periods (S would again approach 1 for all epochs). Therefore, to obtain an accurate estimation of S requires recording the simultaneous activity of dozens of neurons. For our data, the mean r_{pool} across the six recordings was 323 spikes per s with range of 189–609 spikes per s. Given a recording with r_{pool} large enough, the optimal bin size Δt that maximizes the discriminability across brain states was obtained as follows: first, we computed S using different bin sizes Δt (range, 1–1,280 ms; Fig. S1*A*) and calculated its range across all epochs as the difference between maximum and minimum S values (Fig. S1 *B* and *C*, black curves). As we argue above, part of the variation of S could be simply attributed to a variation in r_{pool} across epochs (Fig. S2*A*). To obtain an estimate of the variation of S attributable to pooled rate changes, we computed the homogeneous Poisson silence density (S_{HP}) defined as the probability of finding zero spikes in a bin Δt, assuming that the population spikes in each epoch were generated from a Poisson process with constant rate r_{pool} (Fig. S2*B*, gray). Evaluating the probability mass function of the Poisson distribution at zero (9), one obtains the following:

$$S_{HP} = \exp\left(-\Delta t \cdot r_{pool}\right). \qquad \textbf{[S6]}$$

Next, we computed the range of S_{HP} across epochs and subtracted it from the range of S (Fig. S1 *B* and *C*, blue curve). Thus, for instance, for $\Delta t = 1$ ms the ranges of S and S_{HP} were the same, the difference was zero meaning that $\Delta t = 1$ ms yielded no discriminability of brain state beyond that obtained solely from variations in pooled population rate. We chose the bin size $\Delta t = 20$ ms as the one that maximized the difference between S and S_{HP} ranges averaged across all experiments (Fig. S1*C*, blue curve).

We performed a second control of the impact of pooled rate variations on S by adjusting the bin size Δt in each epoch to correct for the pooled population rate changes. Thus, given the spontaneous pooled rate r_{pool} in each epoch, we found the Δt (Eq. **S6**) that would equalize S_{HP} to the median of the S_{HP} across epochs obtained for $\Delta t = 20$ ms. The S computed with adjusted Δt was only slightly different from S calculated for fixed $\Delta t = 20$ ms (Fig. S2*B*, black and blue curves). Thus, the impact of rate variations on S at $\Delta t = 20$ ms was negligible.

Additionally, we verified that the existent pairwise correlations between neurons increased the probability of observing silent periods. For this, we compared the joint silence density computed from pairs of single-unit spike trains with the product of the silence densities obtained from each spike train separately. We defined the marginal silence density of the ith single unit as $S_i = \langle y_i(t_k)\rangle_{k\in Spon}$, where the binary variable $y_i(t)$ was 1 if $n_i(t;\Delta t) = 0$ and zero otherwise. The joint silence of pair (i,j) was defined as $S_{ij} = \langle y_{ij}(t_k)\rangle_{k\in Spon}$, where $y_{ij}(t)$ was 1 if $n_i(t;\Delta t) + n_j(t;\Delta t) = 0$ and zero otherwise. Fig. S2 *D* and *E* shows the difference $S_{ij} - S_iS_j$ averaged across all pairs vs. bin size Δt.

The instantaneous silence density $S(t)$ computed for evoked activity was obtained by averaging $y(t)$ across stimulus repetitions:

$$S(t) = \left\langle y\left(t^l_{stim} + t\right)\right\rangle_l = \frac{1}{M}\sum_{l=1}^{M} y\left(t^l_{stim} + t\right), \qquad \textbf{[S7]}$$

where t^l_{stim} is the time of the lth stimulus presentation and M is the number of "single-click" stimulus trials assigned to given brain state (see next section). Because $y(t)$ was computed from bins $\Delta t =$ 20 ms whereas for the instantaneous measures of variability [see $FF(t;T)$ and $\rho(t;T)$ below] we used a sliding window $T = 50$ ms, we matched the timescales and "slowed" the instantaneous silence density by convolving $S(t)$ from Eq. **S7** with a square kernel of duration $T = 50$ ms (Fig. 2*B*, and Figs. S4*B*, S8*B*, and S9*G*).

The high activity density H for spontaneous condition was computed similarly to the silence density (Eqs. **S2–S5**) with $y(t) = 1$ whenever $r_{pool}(t)$ was above a given threshold and zero otherwise. We considered two thresholds: one that made H match S during desynchronized epochs (see below), and a second one that made the mean H across epochs match the mean S (Fig. S7*B*, blue and gray traces, respectively). Both thresholds were chosen separately for each experiment.

Brain State Classification. To classify the brain state of each epoch, we used the silence density S computed for the spontaneous activity (Eqs. **S3** and **S5**). We arbitrarily divided the continuum of values spanned by S into three intervals representing three brains states: desynchronized ($S < 0.05$), intermediate ($0.05 \le S \le 0.2$), and synchronized state ($0.2 < S$). Each epoch was classified under one of these states. Each state gathered a sufficient number of stimulus trials M to perform the subsequent analysis of the impact of brain state on the statistics of evoked spiking responses (see below). In our dataset, the total number of single-click trials was on average 1,098 (range, 581–2,175). In particular, the average number of single-click stimulus trials in each brain state was $M = 293$ for the desynchronized (range, 29–419), $M = 370$ for the intermediate (range, 101–652), and $M = 435$ for the synchronized state (range, 128–1,104) (the mean and the range were taken over $n = 6$ experimental sessions). For a given brain state, the data were included for further analysis of evoked activity if we had at least 100 trials, a criterion that only left out the analysis of the desynchronized state from one experiment (it had only $M = 29$ trials).

We checked that the classification of brain state derived from S was consistent to that obtained from a more standard spectral analysis of the LFP (10–13). In particular, we used short-time Fourier transform to compute the power spectrum of the LFP recorded in each channel in epochs of 52.43 s (aligned at the onset with the 50-s epochs used for S). We found that the mean over channels of the LFP power ratio of low frequencies (<5 Hz) over higher frequencies (from 20 to 45 Hz) correlated strongly with S across epochs (see example in Fig. S2 *B* and *C*; mean correlation coefficient across experiments was 0.89; range, 0.78–0.96). Thus, both methods quantified brain state changes similarly.

Spike Count Statistics During Spontaneous and Evoked Activity. To quantify the spike count statistics, rate, Fano factor, and correlation coefficient, we only used spike trains obtained from single units.

Firing rate. For a given unit, stimulus-evoked instantaneous rate averaged across trials was defined as follows:

$$r_i(t) = \frac{1}{T\cdot M}\sum_{l=1}^{M} n_i\left(t^l_{stim} + t;T\right), \qquad \textbf{[S8]}$$

where $n_i(t;T)$ ($i = 1, 2,...,N$) was the spike count of ith neuron in the interval $(t - T/2, t + T/2)$ and t^l_{stim} for ($l = 1, 2,..,M$) was the time onset of the lth single-click trial in the 50-s epochs assigned to one of the three brain states (see above, *Brain State Classification*) and N was a number of single units in a given experiment. We then computed the population-averaged instantaneous rate by averaging across single units as follows:

$$r(t) = \langle r_i(t)\rangle_i = \frac{1}{N}\sum_{i=1}^{N} r_i(t). \qquad \textbf{[S9]}$$

The time courses of the instantaneous rate conditioned on brain state are shown in Fig. 2*A* (one experiment) and Fig. S4*A* (averaged over all experiments).

Fano factor. To quantify the variability in the activity of individual neurons, we computed spike count Fano factor (*FF*) for both spontaneous and evoked conditions. The spike count Fano factor of the *i*th neuron during the spontaneous activity in one epoch was defined as follows:

$$FF_i(T) = \frac{\mathrm{Var}[n_i(t_k;T)]_{k\in Spon}}{\langle n_i(t_k;T)\rangle_{k\in Spon}}, \qquad \textbf{[S10]}$$

where the variance and the mean were taken across the times $\{t_k\}_{k\in Spon}$ corresponding to the center of the bins of size T within the 1.5 s preceding the onset times t^l_{stim} of all of the stimuli occurring in the epoch:

$$\{t_k\}_{k\in Spon} = \left\{ t^l_{stim} - \frac{T}{2}, t^l_{stim} - \frac{3T}{2}, \ldots, t^l_{stim} - T\left(K - \frac{1}{2}\right); l = 1, 2, \ldots, L \right\}. \qquad \textbf{[S11]}$$

The variable K was the number of count windows T in 1.5 s and L was the number of all stimulus trials in the epoch (both single- and double-click presentations were considered, which gave L ranging from 14 to 20 depending on the interstimulus interval). With this notation, the spike count mean and variance in Eq. **S10** can be written as follows:

$$\langle n_i(t_k;T)\rangle_{k\in Spon} = \frac{1}{L\,K}\sum_{l=1}^{L}\sum_{k=1}^{K} n_i\left(t^l_{stim} - \left(k - \frac{1}{2}\right)T; T\right), \qquad \textbf{[S12]}$$

$$\mathrm{Var}[n_i(t_k;T)]_{k\in Spon} = \frac{1}{L\,K}\sum_{l=1}^{L}\sum_{k=1}^{K}\left[n_i\left(t^l_{stim} - \left(k - \frac{1}{2}\right)T; T\right) - \langle n_i(t_k;T)\rangle_k \right]^2. \qquad \textbf{[S13]}$$

Thus, when for instance $T = 50$ ms, the mean and variance were obtained from the spike count in $K{\cdot}L = 420$ or 600 nonoverlapping windows.

The stimulus-evoked instantaneous Fano factor $FF_i(t;T)$ conditioned on brain state was computed differently because the statistics were performed across the stimulus trials from all epochs assigned to one of the three brain states. The instantaneous Fano factor was obtained from the following equation:

$$FF_i(t;T) = \frac{\mathrm{Var}\left[n_i\left(t^l_{stim} + t; T\right)\right]_l}{\left\langle n_i\left(t^l_{stim} + t; T\right)\right\rangle_l}, \qquad \textbf{[S14]}$$

where the mean and the variance were obtained across M single-click presentations in each of the brain state as described by the following:

$$\left\langle n_i\left(t^l_{stim} + t; T\right)\right\rangle_l = \frac{1}{M}\sum_{l=1}^{M} n_i\left(t^l_{stim} + t; T\right), \qquad \textbf{[S15]}$$

$$\mathrm{Var}\left[n_i\left(t^l_{stim} + t; T\right)\right]_l = \frac{1}{M}\sum_{l=1}^{M}\left[n_i\left(t^l_{stim} + t; T\right) - \left\langle n_i\left(t^l_{stim} + t; T\right)\right\rangle_l\right]^2. \qquad \textbf{[S16]}$$

The time course of the stimulus-evoked instantaneous population-averaged Fano factor $FF(t)$, obtained by averaging $FF_i(t)$ over all neurons (similarly to rate in Eq. **S9**), was shown in Fig. S5*A* (for one experiment) and Fig. S5*B* (for average across experiments; $n = 6$ for synchronized and intermediate, $n = 5$ for desynchronized brain state). Because the variance in Eq. **S16** was computed across trials coming from the epochs separated in time during the long recordings (average length, ~2 h), slow drifts in excitability could increase the spike count variance. Therefore, we computed the shift-corrected Fano factor to remove variability due to changes in the excitability of individual neurons occurring in a timescale much slower (e.g., 5–10 min) than the interstimulus interval (14). The shift-corrected Fano factor $\widetilde{FF(t;T)}$ was obtained by substituting the variance in Eq. **S16** by the shift-corrected variance defined as follows:

$$\widetilde{\mathrm{Var}}\left[n_i\left(t^l_{stim} + t; T\right)\right]_l = \frac{1}{M}\sum_{l=1}^{M} n_i\left(t^l_{stim} + t; T\right)^2 - \frac{1}{M-1}\sum_{l=1}^{M-1} n_i\left(t^l_{stim} + t; T\right) n_i\left(t^{l+1}_{stim} + t\right). \qquad \textbf{[S17]}$$

Shift-corrected Fano factor showed identical dependence on brain state and the same stimulus-evoked time courses as $FF(T)$, but with slightly lower values (Fig. S5*C*, average decrease was less than 5% for $T = 50$ ms).

To ease the notation, the explicit dependence of $FF(t;T)$ on T was dropped in the main text and figures becoming $FF(t)$.

Correlation coefficient. Spike count covariability between pairs of single units was quantified using the Pearson correlation coefficient, which, like the Fano factor, was computed separately for spontaneous and evoked conditions. The spike count correlation between the pair of neurons (i,j) during spontaneous activity in a given epoch was obtained from the following:

$$\rho_{ij}(T) = \frac{\mathrm{Cov}\left[n_i(t_k;T), n_j(t_k;T)\right]_{k\in Spon}}{\sqrt{\mathrm{Var}[n_i(t_k;T)]_{k\in Spon} Var\left[n_j(t_k;T)\right]_{k\in Spon}}}. \qquad \textbf{[S18]}$$

Similarly to the Fano factor during spontaneous activity (Eq. **S10**), the covariance and variance were computed across times $\{t_k\}_{k\in Spon}$ (Eq. **S11**). The average correlation coefficient over pairs was then obtained as follows:

$$\rho(T) = \left\langle \rho_{ij}(T)\right\rangle_{ij} = \frac{1}{N(N-1)}\sum_{i=1}^{N}\sum_{j=i+1}^{N}\rho_{ij}(T). \qquad \textbf{[S19]}$$

Fig. 1 shows the population-averaged correlation ρ obtained for $T = 100$ ms as a function of the epochs (Fig. 1*C*) and vs. epoch's spontaneous silence density S (Fig. 1*D*).

The stimulus-evoked instantaneous correlation coefficient $\rho_{ij}(t;T)$ conditioned on brain state was obtained similarly to the instantaneous Fano factor (Eq. **S14**):

$$\rho_{ij}(t;T) = \frac{\mathrm{Cov}\left[n_i\left(t^l_{stim} + t; T\right), n_j\left(t^l_{stim} + t; T\right)\right]_l}{\sqrt{\mathrm{Var}\left[n_i\left(t^l_{stim} + t; T\right)\right]_l \mathrm{Var}\left[n_j\left(t^l_{stim} + t; T\right)\right]_l}}, \qquad \textbf{[S20]}$$

where the covariance and the variance were obtained across all single-click presentations during the epoch assigned to one of three brain states as shown Eqs. **S15** and **S16**. The time course of the evoked population-averaged instantaneous correlation $\rho(t;T)$, obtained by averaging $\rho_{ij}(t;T)$ over all pairs (as in Eq. **S19**), was shown in Fig. 2 *C* and *D* (example experiment) and Fig. S4*C* (average across experiments) for $T = 50$ ms. As with the Fano factor, we also computed the shift-corrected correlation coefficient by replacing the covariance and variance in Eq. **S20** by shift-corrected versions

as described in Eq. **S17**. However, consistent with previous results (14), there were no noticeable systematic differences between the population-averaged standard and shift-corrected correlation coefficients $\rho(t;T)$ computed for $T = 50$ ms.

To ease the notation, the explicit dependence of $\rho(T)$ and $\rho(t;T)$ on T was dropped in the main text and figures becoming ρ and $\rho(t)$.

Surrogate Dataset. This analysis was restricted to the spontaneous activity from 1.5-s intervals preceding each stimulus presentation. We used all single and multiunit spike trains from experimental data to generate a new surrogate dataset from which we quantified the amount of correlation not explained by the occurrence of silent period. First, for each epoch we removed all silent bins detected by the silence variable $y(t) = 1$ (Eq. **S2**; $\Delta t = 20$ ms). Second, we concatenated remaining active periods to obtain a continuous recording with $S = 0$ for each epoch. Third, correlations (Eqs. **S18** and **S19**) were computed in each epoch using the single units identically to what was done for the original data and they were plotted against the density S of each epoch measured in the original data (Fig. 1 *C–F*).

Computational Network Model. We modeled the data assuming that, during spontaneous conditions, the cortical circuit alternates stochastically between an active and a silent network equilibrium points. During active periods, we assumed that the network is in a balanced state where neurons fire weakly correlated Poisson-like spike trains at low firing rate (15). During silent periods, there is barely any firing. Because building such a bistable balanced spiking network is still an open question (*Discussion* in main text), we simplified the problem and modeled the spike count variability as generated by two separate sources (16–20): the first consists in the variation of the population rate $r(t)$ due to alternation between an active and a silent attractors, and the second reflects spiking stochasticity existent at a constant rate. We build a model to investigate the variability of the population rate $r(t)$ (see below) and assumed that all neurons fire conditionally independent Poisson spike trains with rate $r(t)$. To make the problem identifiable and to be able to distinguish firing rate variability from spiking variability, we assumed a separation of timescales between the two sources of variability as the residence times of the network in each equilibria (hundreds of milliseconds) are much longer than timescale of the synaptic current fluctuations triggering spikes (tens of milliseconds). Under these assumptions, one can decompose the variance of the spike count $n_i(t;T)$ of the ith neuron in the interval $(t - T/2, t + T/2)$ as follows:

$$\mathrm{Var}[n_i(t;T)] = \mathrm{Var}\left[\langle n_i(t;T)|r(t)\rangle_{spk}\right] + \left\langle \mathrm{Var}[n_i(t;T)|r(t)]_{spk}\right\rangle, \quad \textbf{[S21]}$$

where the mean (angle brackets) and variance are taken with respect to the spiking variability when indicated with the subscript "*spk*" or with respect to the variability of the rate $r(t)$ otherwise. The expected number of spikes given the rate $r(t)$ is equal to the following:

$$\langle n_i(t;T)|r(t)\rangle_{spk} = \int_{t-T/2}^{t+T/2} r(t')dt' \equiv R(t;T). \quad \textbf{[S22]}$$

Assuming that neurons fire Poisson spike trains, we can substitute the variance of spike counts by the mean:

$$\mathrm{Var}[n_i(t;T)|r(t)]_{spk} = \langle n_i(t;T)|r(t)\rangle_{spk} = R(t;T). \quad \textbf{[S23]}$$

Substituting Eqs. **S22** and **S23** into Eq. **S21**, we obtain that the total variance can be written as follows:

$$\mathrm{Var}[n_i(t;T)] = \mathrm{Var}[R(t;T)] + \langle R(t;T)\rangle. \quad \textbf{[S24]}$$

One can now express the Fano factor $FF_i(t;T)$ as follows:

$$FF_i(t;T) = \frac{\mathrm{Var}[n_i(t;T)]}{\langle n_i(t;T)\rangle} = \frac{\mathrm{Var}[R(t;T)] + \langle R(t;T)\rangle}{\langle R(t;T)\rangle}. \quad \textbf{[S25]}$$

Similarly, we can decompose the spike count covariance between pair of neurons (17):

$$\mathrm{Cov}\left[n_i(t;T), n_j(t;T)\right] = \mathrm{Cov}\left[\langle n_i(t;T)|r(t)\rangle_{spk}, \langle n_j(t;T)|r(t)\rangle_{spk}\right] + \left\langle \mathrm{Cov}\left[n_i(t;T), n_j(t;T)|r(t)\right]_{spk}\right\rangle. \quad \textbf{[S26]}$$

Because we have assumed that all neurons fire with the same rate $r(t)$, the total covariance can be expressed as follows:

$$\mathrm{Cov}\left[n_i(t;T), n_j(t;T)\right] = \mathrm{Var}[R(t;T)] + c_0, \quad \textbf{[S27]}$$

where we have defined c_0 as the mean covariability reflecting spiking stochasticity at a fixed rate:

$$c_0 = \left\langle \mathrm{Cov}\left[n_i(t;T), n_j(t;T)|r(t)\right]_{spk}\right\rangle. \quad \textbf{[S28]}$$

The fact that c_0 does not depend on T means that the spiking covariability was assumed to be instantaneous (i.e., the cross-correlation function conditioned on rate was a Dirac delta). From Eqs. **S24** and **S27**, the correlation coefficient can be expressed as follows:

$$\rho(t;T) = \frac{\mathrm{Var}[R(t;T)] + c_0}{\mathrm{Var}[R(t;T)] + \langle R(t;T)\rangle}. \quad \textbf{[S29]}$$

If we assume that covariations due to spiking stochasticity at a fixed rate are negligible ($c_0 = 0$), the expressions for the spike count Fano factor and the correlation coefficient depend only on the statistics of the population rate $r(t)$. We next present a mechanistic rate model to describe the dynamics of the population rate across brain states and in response to a stimulus.

Statistical Approach to Bistable Model. We performed a statistical analysis of the data asking whether spontaneous population activity has to be described by a bimodal rate distribution, reflecting transition between silent and active periods, or whether in contrast spike count statistics are captured by a model in which silence periods are simply extreme events from a unimodal rate distribution. We assumed a doubly stochastic process where the spike counts $n_i(t;T)$ of the ith neuron ($i = 1, ...N$) in the time interval $(t - T/2, t + T/2)$ were generated according to a Poisson distribution with parameter $\lambda_i = r_i\ T\ G$. For a given epoch (50-s duration), the firing rates r_i were constant, whereas the population gain G was randomly drawn from a probability density function $f(G)$ in each count window $(t - T/2, t + T/2)$. The gain variable G represented network stochastic changes in excitability and as such was common to all cells in the population. Because spike counts $n_i(t;T)$ were conditionally independent given G, correlations in this model were only introduced by the gain variability. Thus, the spike count covariance could be written as follows (Eq. **S26**):

$$\mathrm{Cov}\left[n_i(t;T), n_j(t;T)\right] = \mathrm{Cov}\left[\langle n_i(t;T)|\lambda_i\rangle_{spk}, \langle n_j(t;T)|\lambda_j\rangle_{spk}\right] = \mathrm{Cov}\left[\lambda_i, \lambda_j\right] = r_i r_j T^2 \mathrm{Var}[G]. \quad \textbf{[S30]}$$

In the unimodal model, G followed a gamma distribution with the shape parameter k and scale parameter Q (20) (Fig. S6*B*):

$$f(G;k,Q) = \frac{G^{k-1}\exp(-G/Q)}{\Gamma(k)Q^k}. \quad \textbf{[S31]}$$

We set the mean G to 1 by imposing $Q = 1/k$ such that the mean spike count $\langle n_i(t;T)\rangle = \langle \lambda_i \rangle = r_i T$. We drop hereafter the dependence on Q from $f(G;k,Q)$. The distribution of the spike count $n_i(t;T)$ was a gamma mixture of Poisson distributions, which marginalizing over G yielded a negative binomial distribution (20):

$$P(n;k,q_i) = \frac{\Gamma(n+k)}{\Gamma(n+1)\Gamma(k)} q_i^k (1-q_i)^n, \quad \textbf{[S32]}$$

with $q_i = 1/(1 + r_i T/k)$ and k was a shape parameter of the gain distribution.

To account for bimodality caused by the transitions between silent and active periods, we added to the G distribution $f(G; k)$ a weighted Dirac delta function centered at $G = 0$ (Fig. S6*C*):

$$f_{bim}(G;k,p_s) = p_s \delta(G) + (1-p_s) f(G;k), \quad \textbf{[S33]}$$

where the parameter p_s gives the probability of $G = 0$. In this bimodal model, the spike count probability mass function was a weighted sum of $P(n;k,q_i)$ and the delta Kronecker at zero:

$$P_{bim}(n;k,q_i,p_s) = p_s \delta_{n,0} + (1-p_s) P(n;k,q_i). \quad \textbf{[S34]}$$

Because brain state affected the firing rates r_i and presumably the parameters of gain distribution $f(G)$ (Fig. S6*A*), the two models were fitted separately for each epoch. The parameters of the G distribution, $\{k\}$ for $f(G;k)$ (Eq. **S31**) or $\{k,p_s\}$ for $f_{bim}(G;k,p_s)$ (Eq. **S33**) could then be estimated by fitting $P(n;k,q_i)$ (Eq. **S32**) or $P_{bin}(n;k,q_i,p_s)$ (Eq. **S34**), respectively, to the spike counts $n_i(t;T)$ obtained during spontaneous activity in each epoch. Because under the synchronized brain state the typical silent periods were ~100 ms long, we assumed that changes in G occur in that timescale. Thus, to capture the variability introduced by gain variations, count windows had to be $T = 20$–50 ms because larger windows, e.g., $T \sim 1$–2 s, would partly average out the gain variability. Due to low individual average rates ($r_i \sim 2$–3 spikes per s), the counts $n_i(t;T)$ using $T = 20$–50 ms were effectively binary and never did exhibit bimodality regardless the brain state (Fig. S6*D*). As a result, the fitted functions $P(n;k,q_i)$ (Eq. **S32**) and $P_{bin}(n;k,q_i,p_s)$ (Eq. **S34**) were similar, preventing the discrimination between the two models (Fig. S6*D*). Because in the model the gain was common to all neurons, the spike count of the pooled activity of N neurons $n_{pool}(t;T) = \sum_{i=1}^{N} n_i(t;T)$ followed, given G, a Poisson distribution with parameter $\lambda = r_{pool} T G$, where $r_{pool} = \sum_{i=1}^{N} r_i$. Therefore, we fitted the functions $P(n;k,q_{pool})$ (Eq. **S32**) and $P_{bin}(n;k,q_{pool},p_s)$ (Eq. **S32**), with $q_{pool} = 1/(1 + r_{pool} T/k)$, to the spike counts $n_{pool}(t;T)$ obtained from pooling all of the simultaneously recorded single and multiunit spike trains (Fig. S6*E*). We used a simplex algorithm (the Matlab function *fminsearch*) that searched for the values of $\{k,q_{pool}\}$ or $\{k,q_{pool},p_s\}$ that minimized the negative log-likelihood of the set of counts $\{n_{pool}(t;T)\}$ (Fig. S6*A*, blue arrows). From this fit, we then obtained the G distributions $f(G;k)$ and $f_{bim}(G;k,p_s)$ (Fig. S6 *B* and *C*).

We tested which model better reproduced the population spike count variability. For the unimodal model, the variance of the population spike count was obtained from the negative binomial distribution $P(n;k,q_{pool})$:

$$\mathrm{Var}(n_{pool}) = \frac{(1-q_{pool})k}{q_{pool}^2}. \quad \textbf{[S35]}$$

For the bimodal case, it is easy to show that the variance of the count is given by the following:

$$\mathrm{Var}(n_{pool}) = \frac{(1-p_s)(1-q_{pool})k}{q_{pool}^2} + \frac{p_s(1-p_s)(1-q_{pool})^2 k^2}{q_{pool}^2}. \quad \textbf{[S36]}$$

Both models reproduced accurately the mean counts, but the unimodal model significantly overestimated the count variance in comparison with bimodal model (compare gray and blue dots in Fig. S6*F*). This underdispersion of the data compared with the unimodal model was greater for synchronized epochs (Fig. S6*F*). A similar behavior was observed in all ($n = 6$) experimental datasets. The bimodal model was a better predictor of the experimental mean pairwise spike count covariance (Fig. S6*G*). For both models, the pairwise spike count covariance was computed for each single-unit pair using equation Eq. **S30** and then averaged across pairs.

To assess the models' relative goodness-of-fit, we divided the set of counts $\{n_{pool}(t;T)\}$ of each epoch in two halves [odd and even windows $(t - T/2, t + T/2)$], fitted the models using the first half and quantified the likelihood of the second half. We then normalized the likelihood by the total number of spikes $\sum_{t \in even} n_{pool}(t;T)$ so that it was expressed per spike. We repeated the same procedure switching the two halves and computed the mean of the two likelihoods (Fig. S6*H*). In desynchronized epochs, when $S \sim 0$, both models were equally accurate predicting the data (Fig. S6 *E*, *Left*, and *H*, brown dots). However, as S increased, the histogram of $n_{pool}(t;T)$ became progressively bimodal and the likelihood of the bimodal model became larger than that of the unimodal model (Fig. S6 *E* and *H*, orange and red dots). In synchronized epochs, the difference between the two models, expressed as a log-likelihood ratio (LLR), varied nonmonotonically with count window T (Fig. S6*H*, *Inset*, filled squares). For a very small T, the spike counts became binary, which made two models similar. On the other hand, as T grew above 50 ms, the number of silence periods approached zero (Fig. S1*A*), which made $p_s \sim 0$ and, as a result, the two models became equivalent.

To demonstrate that correlations were necessary for the population data to be bimodal, we destroyed the time relationships across units by randomly and independently shifting each spike train. As expected, in this surrogate data without correlations among neurons, the fitted models were equally likely independently of the size of counting window T (Fig. S6*H*, *Inset*, open squares). The discrimination between two models also depended on the number of units merged to obtain $n_{pool}(t;T)$. Fitting the models to only one unit was similar to using a very small count window T because spike count was a binary variable (Fig. S6 *B* and *I*, light gray dots). When the activity of more neurons was pooled, the LLR of the two models showed a monotonic increase with silence density S (Fig. S6*I*). Thus, the more neurons recorded simultaneously, the easier is to establish the bimodality of the population spike counts. To obtain LLR presented in Fig. S6*I*, we fitted both models to 50 randomly chosen subpopulations of N units and computed the mean.

Population Rate Dynamics in the Bistable Model. We studied the dynamics of the population of excitatory neurons using rate model

with adaptation (21, 22). The dynamics of the population rate $r(t)$ and adaptation $a(t)$ were given by the following equations:

$$\tau_r \frac{dr}{dt} = -r(t) - \varphi(\alpha r(t) - a(t) + I(t) - \theta), \qquad \textbf{[S37]}$$

$$\tau_a \frac{da}{at} = -a(t) + \beta r(t),$$

where the external input $I(t) = I + stim(t) + \sigma\xi(t)$ was composed of a constant term I (range, 0–4 a.u.), the stimulus modeled as a step function $stim(t) = 60$ a.u. for $0 < t < 10$ ms and zero otherwise (Fig. 4). We hereafter omit specifying the units when they are arbitrary, that is a.u. should be assumed if no units are specified. In Fig. S8, we used stimuli of different amplitude (range, 10–500) and different duration (range, 5–50 ms). The noise term was modeled as an Ornstein–Uhlenbeck process $\xi(t)$ with zero mean, SD $\sigma = 4.5$ (Figs. 3 and 4, and Figs. S7 and S8), and time constant of 0.5 ms. The rate activation threshold was $\theta = 2$. The rate and adaptation time constants were set to $\tau_r = 5$ ms and $\tau_a = 250$ ms, respectively. The strength of recurrent feedback was $\alpha = 4.6$ s and the strength of adaptation β was varied in the range of 0.3–3 s. Rate model equations (Eq. **S37**) were numerically integrated using a fourth-order Runge–Kutta method with integration time step $dt = 0.005$ ms.

The transfer function $\varphi(x)$ was given by the following (23):

$$\varphi(x) = \begin{cases} 0, & x < 0 \\ gx^2, & 0 \le x \le 1 \\ g\sqrt{4x-3}, & x > 1 \end{cases}. \qquad \textbf{[S38]}$$

In the quoted study (23), the gain constant was set to $g = 10$ to approximately fit the *f–I* curve of cortical pyramidal cells. We used $g = 0.45$ Hz (Figs. 3 and 4, and Figs. S7 and S8) to match the rate of the model's active attractor with the mean population rate observed in the data (~3 spikes per s). This rescaling did not alter the dynamics of the system but only changed the values of the rate $r(t)$ during active periods. Because the rate during silent periods was close to zero independently of g, increasing g increased the difference between the silent and active rates, i.e., increased population rate variance, and consequently increased the correlation $\rho(T)$ (Eq. **S29**).

To investigate the minimal model reproducing the dynamics of evoked correlation, we simplified our model by removing adaptation (i.e., setting $\beta = 0$ in Eq. **S37**) (Fig. S9, bistable model). To obtain baseline values of the rate and silence density comparable to the bistable model with adaptation, we set $I = 1.36$, $\sigma = 2.8$, $\alpha = 2.25$ s, and $g = 0.6$ Hz. We also modeled the impact of short-term synaptic depression on the thalamocortical afferents by adding an after-stimulus suppression term: $I(t) = I + stim(t) - \Theta(t - t_{off})D \exp(-(t - t_{off})/\tau_{rec}) + \sigma\xi(t)$, where $t_{off} = 10$ ms is the time of the stimulus offset, $\Theta(t)$ is a Heaviside function, the suppression amplitude is $D = 0.3$ or 0.6, and the recovery time constant is $\tau_{rec} = 75$ ms.

Population Rate Dynamics in the Gaussian Model. To implement a Gaussian monostable model describing population activity, we used the same rate dynamics as in the bistable model (Eq. **S37**) with no adaption ($\beta = 0$) and a threshold-linear transfer function given by the following:

$$\varphi_{TL}(x) = \begin{cases} 0, & x < 0 \\ g_{TL}x, & x \ge 0 \end{cases}. \qquad \textbf{[S39]}$$

The value of the only stable fixed point obtained in this model was matched to the rate of active attractor of the bistable model by setting $I = 7.5$, $\alpha = 2.25$ s, and $g_{TL} = 0.2$ Hz. To obtain levels of silence density comparable to the bistable model, we set the noise time constant to 5 ms and varied the fluctuations amplitude σ from 2 to 16 (Fig. S7). For the intermediate brain state presented in Fig. S9, the amplitude was $\sigma = 9$. As in the minimal model without adaptation described above, we introduced an after-stimulus suppression term to reproduce the dynamics of evoked correlation with suppression amplitude $D = 2$ and 5, and recovery constant $\tau_{rec} = 75$ ms (Fig. S9; monostable model).

Analysis of the Rate Model in Spontaneous Conditions. To simulate spontaneous activity in the model we set $stim(t) = 0$. For each combination (β, I), we run the model for 500 s (Fig. 3) and computed the mean rate by averaging $r(t)$ across time (Fig. 3*D*, *Left*). We calculated the silence density S (Fig. 3*D*) as the fraction of time in which $r(t) < 0.9$ Hz (Fig. 3) or $r(t) < 1$ Hz (Fig. S7*F*). The high activity density H was computed as a fraction of time in which $r(t)$ was above certain threshold: 3 and 3.9 Hz for the monostable model (Fig. S7*F*) and 2.9 and 3.1 Hz for the bistable model (Fig. S7*G*). To obtain the correlation $\rho(T)$ (Eq. **S29**), we computed $R(t;T)$ by convolving $r(t)$ with a square kernel (Eq. **S22**; width $T = 100$ ms; amplitude, 1) and calculated its mean and variance across time. We used $c_0 = 0$ (Fig. 3*D*) except in Fig. 3*E* where we also used $c_0 = 0.01$ (Fig. 3*E*, black line). We explored the parameters plane (β, I) to study the relation between S and ρ. Relatively big values of β and small values of I gave $S > 0.5$, which was not observed in our datasets. At small β, increasing I reproduced the silence density vs. correlation relationship observed across brain states (Fig. 3*E*). Similar relationship could be obtained by the simultaneous increase of I and the decrease of β (Fig. 3 *D* and *E*).

If the spike count window T is much smaller than the mean silent and active period durations, one can simplify the problem and assume that the variable $R(t;T)$ only takes the values 0 (during silent periods) and $r_{act}T$ (during active periods) with probabilities S and $1 - S$, respectively (i.e. the probability of T straddling between a silent and an active period is negligible). Here, r_{act} is the population rate during active periods. The variance $\mathrm{Var}[R(t;T)] = S(1 - S)(r_{act}T)^2$ and the mean $\langle R(t;T)\rangle = (1 - S)(r_{act}T)^2$ can then be used in to derive $\rho(T)$ (Eq. **S29**) with $c_0 = 0$ that can be expressed as follows:

$$\rho(T) = \frac{Sr_{act}T}{1 + Sr_{act}T}. \qquad \textbf{[S40]}$$

Given that in the data and in the model $r_{act} \sim 3$ spikes per s and $S < 0.5$, for $T = 100$ ms the product $r_{act}\,T\,S << 1$ and Eq. **S33** becomes the following:

$$\rho(T) \simeq Sr_{act}T, \qquad \textbf{[S41]}$$

which reveals a linear relationship between $\rho(T)$ and S with slope $r_{act}T$. This simple expression gave a relatively good prediction of the relation between $\rho(T)$ and S in the model. Notice, however, that in general $\rho(T)$ is not a function of only S because different mean silent and active period durations can yield different correlation at the same S value (Fig. 3*E*, gray shaded area).

Analysis of the Rate Model in Evoked Conditions. To model the responses to click stimuli, we set $stim(t) = 60$ for $0 < t < 10$ ms and zero otherwise (Fig. 4). The instantaneous mean rate, silence density, integrated rate variance, and correlation (Fig. 4 and Figs. S8 and S9) were obtained across 10,000 stimulus repetitions. We compare the model traces with those obtained from data, and we computed the mean evoked rate as the expected spike count normalized by the count window size T (Fig. 4*A* and Figs. S8*A* and S9*F*, and Movies S1 and S2):

$$r(t;T) = \frac{\langle n(t;T)\rangle}{T} = \frac{\left\langle \langle n(t;T)|r(t)\rangle_{spks} \right\rangle_r}{T} = \frac{\langle R(t;T)\rangle_r}{T}, \qquad \textbf{[S42]}$$

where $R(t;T)$ is the expected number of spikes conditioned on $r(t)$ (also termed integrated rate; Eq. **S22**). Moreover, we

plotted the variance Var[$R(t;T)$] (Fig. 4*C* and Figs. S8*C* and S9*H*; Movies S1 and S2) to illustrate the variability introduced by the rate $r(t)$ (we used $T = 50$ ms). Instantaneous silence density $S(t)$ was computed as the fraction of trials in which the rate $r(t) < 0.9$ Hz (Fig. 4*B* and Fig. S8*B*) or $r(t) < 1$ Hz (Fig. S9*G*). For plotting purposes, we matched the timescales of the instantaneous silence density and spike count statistics by convolving $S(t)$ with a square kernel of duration $T = 50$ ms (Fig. 4*B* and Figs. S8*B* and S9*G*). The instantaneous spike count correlation $\rho(t;T)$ (Fig. 4*D* and Figs. S8*D* and S9*I*; Movies S1 and S2) was computed from Eq. **S29** with $c_0 = 0$ using a window $T = 50$ ms.

1. Sally SL, Kelly JB (1988) Organization of auditory cortex in the albino rat: Sound frequency. *J Neurophysiol* 59(5):1627–1638.
2. Doron NN, Ledoux JE, Semple MN (2002) Redefining the tonotopic core of rat auditory cortex: Physiological evidence for a posterior field. *J Comp Neurol* 453(4):345–360.
3. Rutkowski RG, Miasnikov AA, Weinberger NM (2003) Characterisation of multiple physiological fields within the anatomical core of rat auditory cortex. *Hear Res* 181(1-2):116–130.
4. Harris KD, Henze DA, Csicsvari J, Hirase H, Buzsáki G (2000) Accuracy of tetrode spike separation as determined by simultaneous intracellular and extracellular measurements. *J Neurophysiol* 84(1):401–414.
5. Takekawa T, Isomura Y, Fukai T (2012) Spike sorting of heterogeneous neuron types by multimodality-weighted PCA and explicit robust variational Bayes. *Front Neuroinform* 6:5.
6. Takekawa T, Isomura Y, Fukai T (2010) Accurate spike sorting for multi-unit recordings. *Eur J Neurosci* 31(2):263–272.
7. Hazan L, Zugaro M, Buzsáki G (2006) Klusters, NeuroScope, NDManager: A free software suite for neurophysiological data processing and visualization. *J Neurosci Methods* 155(2):207–216.
8. Sakata S, Harris KD (2012) Laminar-dependent effects of cortical state on auditory cortical spontaneous activity. *Front Neural Circuits* 6:109.
9. Papoulis A, Pillai SU (2002) *Probability, Random Variables, and Stochastic Processes* (McGraw-Hill, Boston).
10. Mukovski M, Chauvette S, Timofeev I, Volgushev M (2007) Detection of active and silent states in neocortical neurons from the field potential signal during slow-wave sleep. *Cereb Cortex* 17(2):400–414.
11. Goard M, Dan Y (2009) Basal forebrain activation enhances cortical coding of natural scenes. *Nat Neurosci* 12(11):1444–1449.
12. Li C-YT, Poo M-M, Dan Y (2009) Burst spiking of a single cortical neuron modifies global brain state. *Science* 324(5927):643–646.
13. Marguet SL, Harris KD (2011) State-dependent representation of amplitude-modulated noise stimuli in rat auditory cortex. *J Neurosci* 31(17):6414–6420.
14. Bair W, Zohary E, Newsome WT (2001) Correlated firing in macaque visual area MT: Time scales and relationship to behavior. *J Neurosci* 21(5):1676–1697.
15. Renart A, et al. (2010) The asynchronous state in cortical circuits. *Science* 327(5965): 587–590.
16. Shadlen MN, Newsome WT (1998) The variable discharge of cortical neurons: Implications for connectivity, computation, and information coding. *J Neurosci* 18(10): 3870–3896.
17. Staude B, Rotter S, Grün S (2008) Can spike coordination be differentiated from rate covariation? *Neural Comput* 20(8):1973–1999.
18. Churchland MM, et al. (2010) Stimulus onset quenches neural variability: A widespread cortical phenomenon. *Nat Neurosci* 13(3):369–378.
19. Churchland AK, et al. (2011) Variance as a signature of neural computations during decision making. *Neuron* 69(4):818–831.
20. Goris RLT, Movshon JA, Simoncelli EP (2014) Partitioning neuronal variability. *Nat Neurosci* 17(6):858–865.
21. Latham PE, Richmond BJ, Nelson PG, Nirenberg S (2000) Intrinsic dynamics in neuronal networks. I. Theory. *J Neurophysiol* 83(2):808–827.
22. Mattia M, Sanchez-Vives MV (2012) Exploring the spectrum of dynamical regimes and timescales in spontaneous cortical activity. *Cogn Neurodyn* 6(3):239–250.
23. Brunel N (2003) Dynamics and plasticity of stimulus-selective persistent activity in cortical network models. *Cereb Cortex* 13(11):1151–1161.

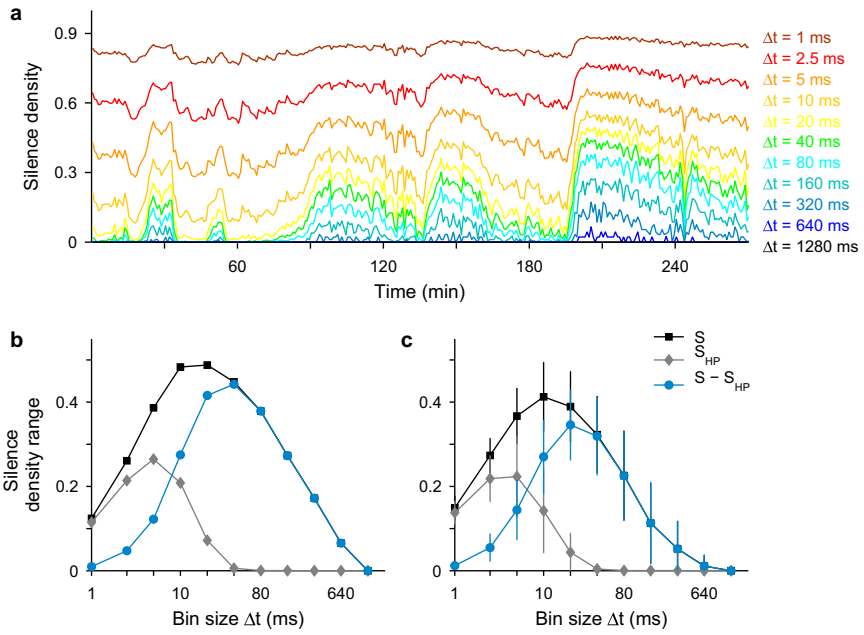

Fig. S1. Silence density depends on the bin size used to detect silence. (*A*) Variations of silence density S (Eq. **S5**) across one example experiment obtained using different bin sizes Δt (see values in *Inset*). S was computed in 50-s epochs. As Δt decreases S approaches 1 (red colors), whereas as Δt increases S goes to zero (blue colors). In both the small and large Δt limits, the range spanned by S throughout the experiment is small. (*B*) The ranges of S (black) and homogeneous Poisson silence density S_{HP} (gray), defined as the difference between maximum and minimum values spanned during the experiment, as a function of Δt. The S_{HP} (Eq. **S6**) gives the expected silence density produced in each epoch by a homogeneous Poisson process with a rate matching the pooled population spike rate R. Variations in S_{HP} thus reflect the changes in r_{pool} accompanying brain state changes (Fig. S2*A*). The difference between the ranges of S and S_{HP} is also shown (blue). (*C*) As in *B*, but for the average over $n = 6$ experiments (error bars show SD). For further analyses, we chose $\Delta t = 20$ ms as the bin size that maximizes the averaged difference between the range of S and S_{HP}.

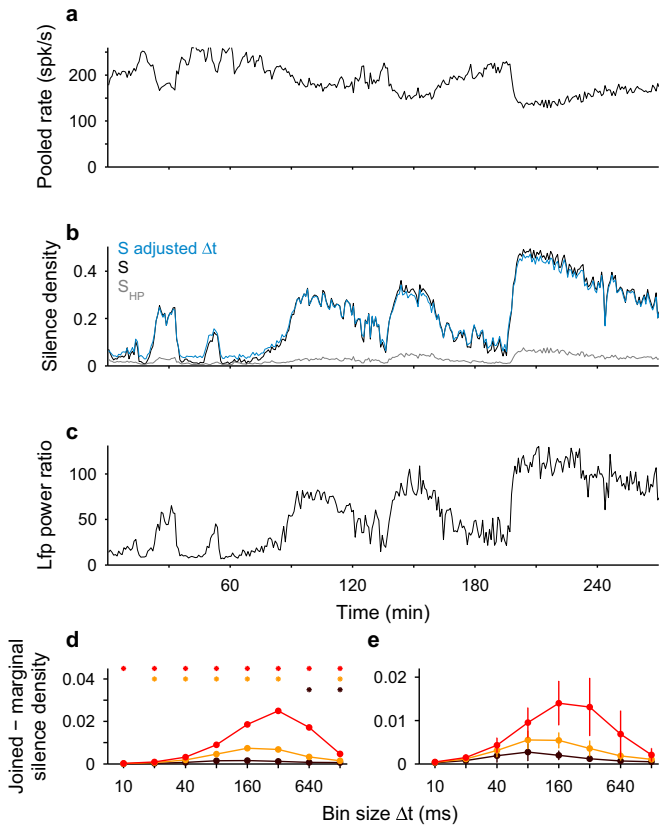

Fig. S2. Variations in silence density cannot be accounted by changes in population rate. (*A*) Pooled population firing rate r_{pool} computed in 50-s epochs from one example experiment (also shown in Figs. 1 and 2). Note that the pooled population rate (Eq. **S1**) is not normalized by the number of single-unit and multiunit spike trains ($n = 84$). (*B*) Silence density S (black; Eq. **S5**) and homogeneous Poisson silence density S_{HP} (gray; Eq. **S6**) computed for each epoch using bins of $\Delta t = 20$ ms. Silence density computed with adjusted Δt (to compensate for the changes in rate r_{pool}) is shown in blue. (*C*) Mean LFP power ratio defined as the fraction of spectral density at low frequencies (<5 Hz) over higher frequencies (from 20 to 45 Hz). The mean computed across recording channels ($n = 60$). In this experiment, the correlation coefficient between mean LFP power ratio and S across epochs (for $\Delta t = 20$ ms) was $r = 0.96$ (mean across all experiments was 0.89; range, 0.78–0.96). (*D*) Difference between joint silence density obtained from cell pairs and the product of their marginal densities, $S_{ij} - S_iS_j$, vs. bin size Δt. The difference was averaged across cell pairs ($i \neq j$; $n = 3{,}240$) by grouping desynchronized (brown), intermediate (orange), and synchronized (red) epochs. Data came from the experiment shown in *A*–*C*. Stars above indicate points significantly different from zero (Wilcoxon rank-sum test, $P < 0.05$). (*E*) Same as *D*, but averaged across experiments ($n = 6$; error bars show SD).

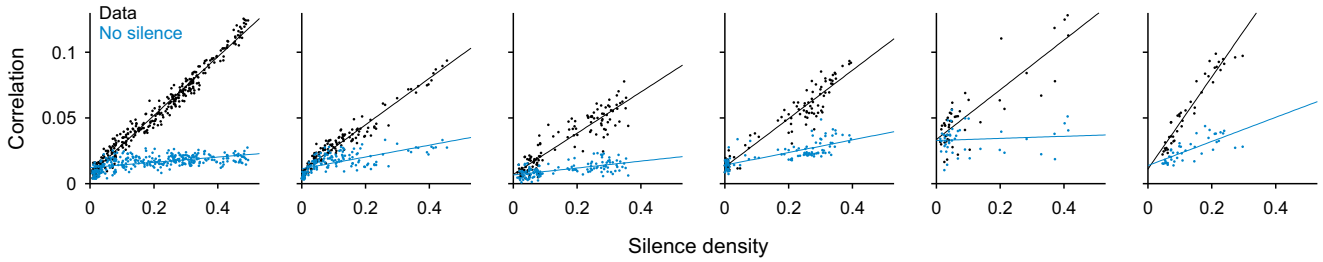

Fig. S3. The relation between correlations and silence density during spontaneous activity for individual experiments. Averaged spontaneous spike count correlation ρ vs. silence density S obtained for six experiments (the leftmost panel corresponds to the experiment shown in Fig. 1*D*). Correlations were averaged over pairs of recorded single units (black; count window $T = 100$ ms) and surrogate data (blue) obtained by removing all silent periods. Each dot represents a 50-s epoch. Linear fits from experimental and surrogate data (lines) have slopes in the ranges of 0.16–0.35 and 0.008–0.091, respectively. The intercepts ranges are 0.007–0.03 (data) and 0.011–0.32 (surrogates).

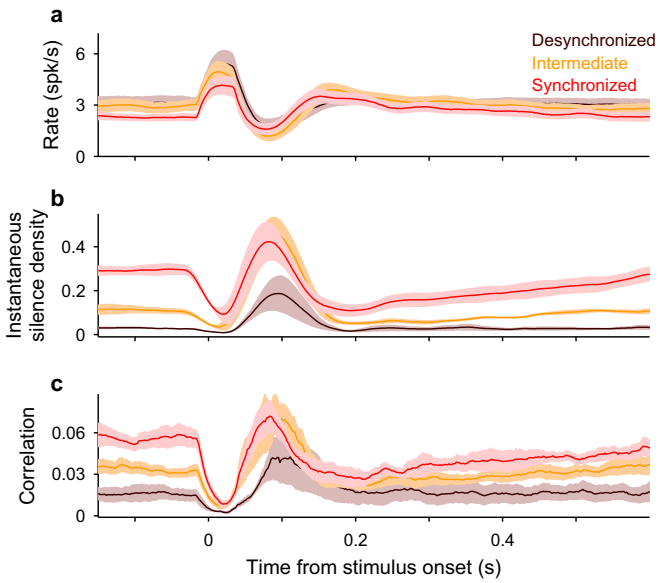

Fig. S4. Dynamics of the evoked response in A1 across brain states. (*A*–*C*) Population-averaged instantaneous rate $r(t)$ (*A*), instantaneous silence density $S(t)$ (*B*), and instantaneous correlation $\rho(t;T)$ (*C*) in response to a click stimulus during desynchronized (brown), intermediate (orange), and synchronized (red) epochs. For each experiment, the statistics were obtained across stimulus repetitions within the given brain state. Population rate was averaged across single units and correlation was average across single-unit pairs. Panels show the mean over experiments ($n = 6$ for synchronized and intermediate state; $n = 5$ for desynchronized state). Rate and correlation were obtained using $T = 50$-ms sliding windows (time step, 2 ms). The density $S(t)$ was obtained using bins $\Delta t = 20$ ms, and then it was smoothed with a square kernel of width $T = 50$ ms (Eq. **S7**). Shaded areas show the SEM.

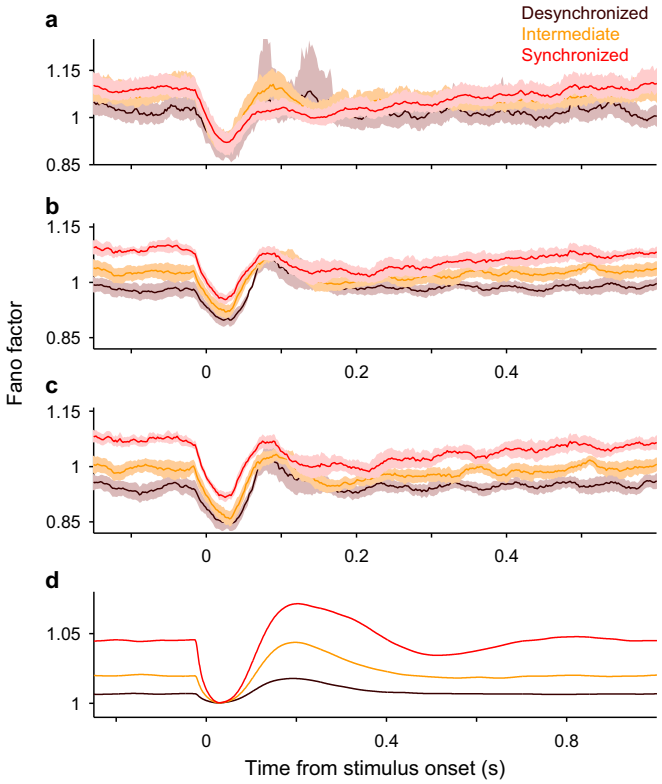

Fig. S5. Evoked dynamics of Fano factor for experimental and model data. (*A*) Population-averaged instantaneous Fano factor $FF(t;T)$ from one example experiment session (*A*, same experiment as in Figs. 1 and 2 and Figs. S1 and S2) in response to a click stimulus during desynchronized (brown), intermediate (orange), and synchronized (red) epochs. The statistics were obtained across stimulus repetitions under the corresponding state using $T = 50$-ms sliding windows (step, 2 ms; Eq. **S14**) and then averaged over single units ($n = 81$ units; shaded area illustrates 95% confidence bands obtained from 500 random resamples). (*B*) Average over all experiments of the population-averaged Fano factor shown in *A* ($n = 6$ for synchronized and intermediate state, $n = 5$ for desynchronized state; shaded area represents SEM). (*C*) Same as in *B* but for the $FF(t;T)$ computed using the shift-corrected variance (Eq. **S17**) that factors out the variability due to slow variations in neuronal excitability. (*D*) Stimulus-evoked instantaneous Fano factor computed from numerical simulations of the computational rate model for the three brain states defined in Fig. 3 (same color code). Statistics was obtained across repeated stimulus presentations (Eq. **S25**). Stimulus was a 10-ms square pulse added to the external input $I(t)$. Notice the different temporal scale used in *A*–*C* and *D*.

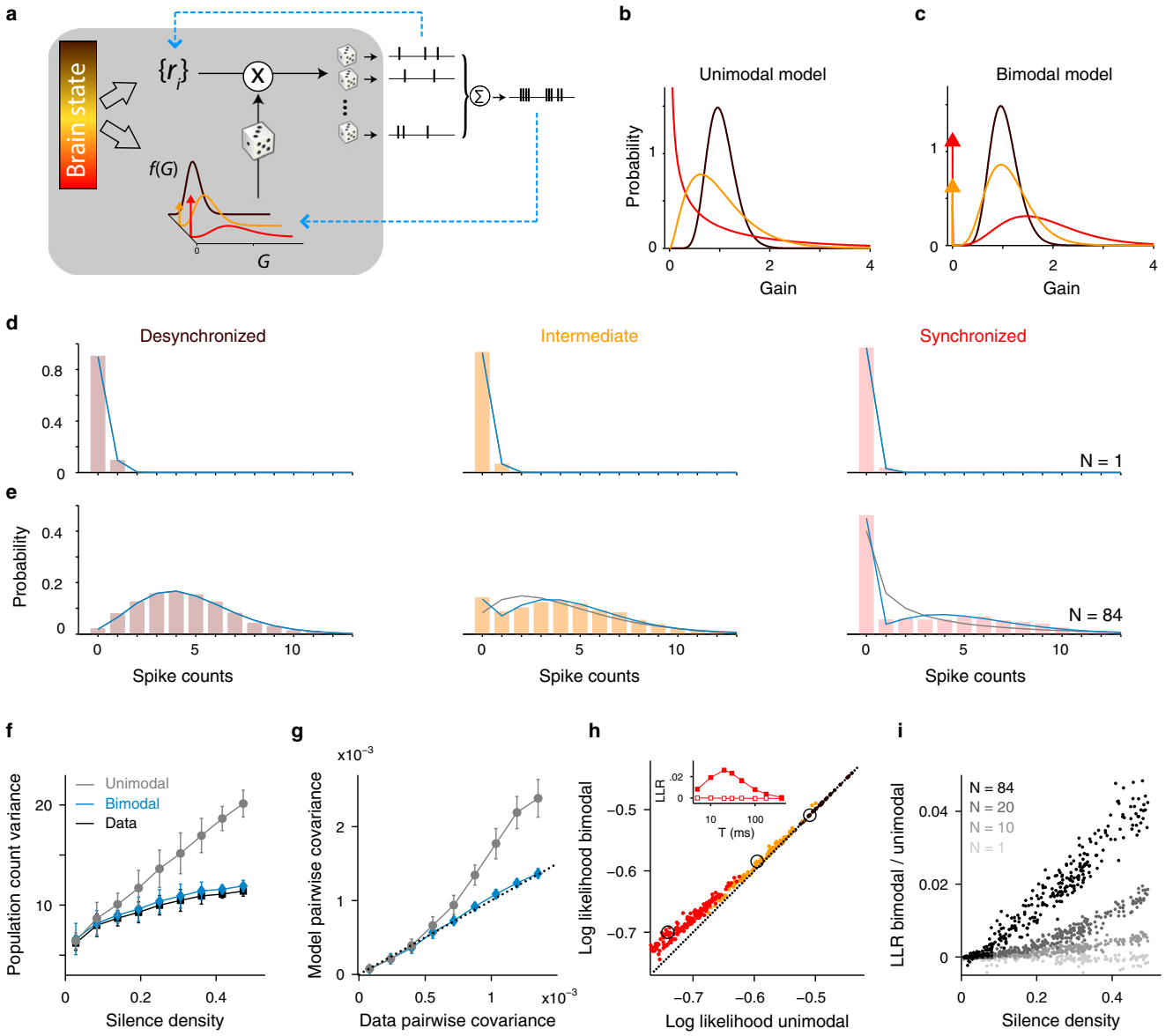

Fig. S6. Unimodal vs. bimodal models of spike count statistics across brain states. (*A*) Model diagram. Given the population gain G, the spike counts $n_i(t;T)$ in the time interval $(t - T/2, t + T/2)$ for each neuron ($i = 1, \ldots, N$) are generated according to a Poisson distribution with parameter $r_i\ T\ G$. The firing rates r_i are constant in each epoch, whereas G is randomly drawn, in each count window $(t - T/2, t + T/2)$, from a probability density function $f(G)$. Brain state variations affect the rates r_i and the gain distribution $f(G)$ (*Left*). Thus, changes in G occur in a timescale (~100 ms) that is faster than changes in brain state (~1–2 min) but slower than the spiking stochasticity (a few milliseconds). Because spike counts $n_i(t;T)$ are conditionally independent given G, correlations are only introduced by the gain variability. (*B*) Probability density function $f(G)$ for the unimodal model in three epochs representative of desynchronized (brown), intermediate (yellow), and synchronized (red) brain states. The $f(G)$ is a Gamma distribution obtained by fitting the unimodal model to the population spike counts obtained from spontaneous activity (merge of $n = 84$ single units and multiunits; $T = 20$ ms; blue bottom arrow in *A*; see *SI Methods* for details). (*C*) Same as in *B* but for a bimodal model where $f(G)$ consists of a Gamma distribution plus a Dirac delta function at zero (vertical arrows). The amplitude of the delta function obtained from the fit was approximately equal to S in each epoch (delta amplitudes in the plot are set for illustration purposes only). (*D*) Spike count histograms for an example neuron in the three selected epochs (bars) together with the distribution predicted from the unimodal (gray line) and bimodal (blue line) models shown in *B* and *C*. Because the rates of single neurons are low (e.g., mean rate across epochs for this neuron was $r_i = 3.9$ spikes per s), spike counts are effectively binary and both models give similar distributions that are almost independent of the brain state. (*E*) Population spike count histograms ($N = 84$; mean rate across epochs, 189 spikes per s) and the predictions from the models shown in *B* and *C*. Color code as in *D*. Data come from the same experiment shown in Figs. 1 and 2. During desynchronized epochs ($S \sim 0$), histograms are unimodal and both models give equivalent fits (blue and gray lines overlap). With cortical synchronization, S increases, the histograms become progressively more bimodal, and the bimodal model fitted the data more accurately than the unimodal model. (*F*) Mean population spike count variance for the experimental data and for the two fitted models vs. silence density (color code defined in *Inset*). The mean and SD (error bars) are taken across epochs with given silence density. Although the bimodal model predicts the variance across all brain states, the unimodal model overestimates spike count variability particularly as brain state becomes synchronized. The same qualitative relation was observed in all experiments ($n = 6$). (*G*) Mean pairwise spike count covariance derived from the models vs. the covariance obtained from the data ($n = 3{,}240$ single-unit pairs). As in *F* during synchronized epochs the unimodal model overestimates covariance. (*H*) Predictive accuracy of the unimodal vs. bimodal models across epochs. Each data point illustrates the log-likelihood of the population counts of one epoch. In each epoch, models were fitted to the half of data, and log-likelihood was computed on the remaining half and expressed per spike (*SI Methods*). Epochs were colored according to the three brain state categories defined in *Methods*. (*Inset*) Log-likelihood ratio (LLR) of bimodal over unimodal model, averaged across synchronized epochs, vs. count window T (filled symbols). The

Legend continued on following page

bimodality of the data was optimally revealed using T in the range of 10–50 ms. If the time relationships across units was removed by randomly and independently shifting each spike train, the data were no longer bimodal (open symbols). (*I*) LLR between bimodal and unimodal models in each epoch as a function of S. The models were fitted to population counts obtained from a subpopulation of N randomly chosen neurons (*Inset*). The growth in bimodality with S is harder to detect in subpopulations of small N.

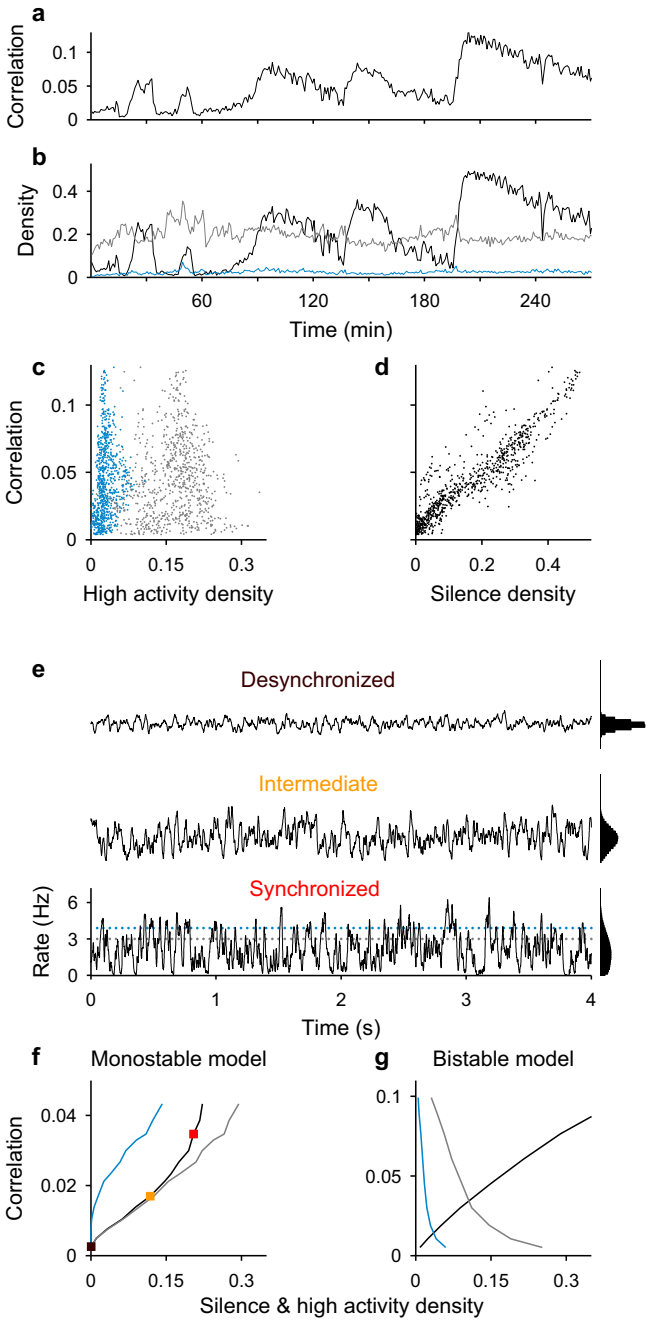

Fig. S7. Comparison of Gaussian and bistable models describing spontaneous changes in correlation. (*A*) Averaged spontaneous spike count correlations ρ obtained across 50-s epochs (same experiment as Fig. 1). (*B*) Silence density S (black) and high activity density H, with average matching the average S (gray; H threshold of 6 spikes in a bin $\Delta t = 20$ ms) or matching S at the most desynchronized epochs (blue; H threshold, 10 spikes). (*C*) Correlation vs. H for all $n = 6$ experiments. Each dot represents a 50-s epoch. H thresholds were chosen separately for each experiment. Note the lack of systematic relation between ρ and H (mean ρ–H correlation coefficient across experiments were −0.03 and 0.24 for gray and blue sets, respectively). (*D*) Correlation vs. S for all experiments ($n = 6$) shows a clear linear relationship (mean ρ–S correlation coefficient was 0.94). (*E*) Spontaneous activity traces (*Left*) and rate histograms (*Right*) for Gaussian model for three amplitudes of the input fluctuations σ (3, 8, 14) chosen to reproduce different brain states. (*F*) Correlation vs. S (black) and vs. H (gray and blue) obtained in the monostable model across brain states, modeled by changing σ (range, 2–16). Two H thresholds were used (3 and 3.9 Hz; dotted lines in *E*) to compare two sets of high activity density as in *B* and *C*. Colored squares mark the ρ–S values corresponding to the states shown in *E*. The Gaussian model shows an increase of both densities in disagreement with the ρ–H behavior found in the data (*C*). (*G*) Same as *F* for the bistable model. Brain state changes were modeled by changing I as in Fig. 3 *E* and *F* (range $I = 0.4$–4). Curve ρ–S (black) is taken from Fig. 3*E* (gray). High activity thresholds were 2.9 Hz (gray) and 3.1 Hz (blue).

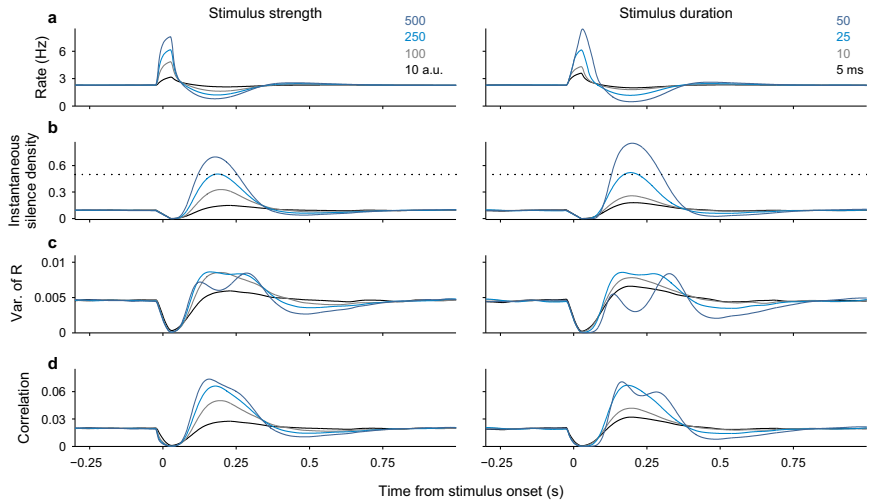

Fig. S8. Correlation evoked dynamics for different stimulus parameters. (*A*–*D*) Stimulus-evoked mean instantaneous rate $r(t)$ (*A*), instantaneous silence density $S(t)$ (*B*), variance of integrated rate $R(t)$ (*C*), and instantaneous correlation $\rho(t)$ (*D*) obtained for the bistable network with adaptation operating in the intermediate brain state (same as orange trace in Fig. 4 *A*–*D*). Statistics were obtained across repeated presentations of the pulse stimulus using different amplitudes (*Left*; *Inset*) and different durations (*Right*; *Inset*). Stimuli with larger amplitude or duration caused a larger evoked response $r(t)$ and, due to the larger recruitment of adaptation, a deeper poststimulus rate suppression (*A*). This increased suppression was caused by more pronounced rebound in $S(t)$ (*B*) and yielded a larger rebound in $\rho(t)$ followed by a deeper second drop (*D*). Notice that the rebound amplitude of the integrated rate variance increases until $S(t)$ reaches 0.5 (dotted line in *B*). For $S(t) > 0.5$, the variance decreases (see small drop in the rebound for the largest stimulus amplitude or duration; dark blue traces in *C*). This drop at the rebound is mitigated in $\rho(t)$ by the decrease of the mean rate (*D*) and only becomes apparent when $S(t)$ peaks at very high amplitudes (dark blue traces in right panels).

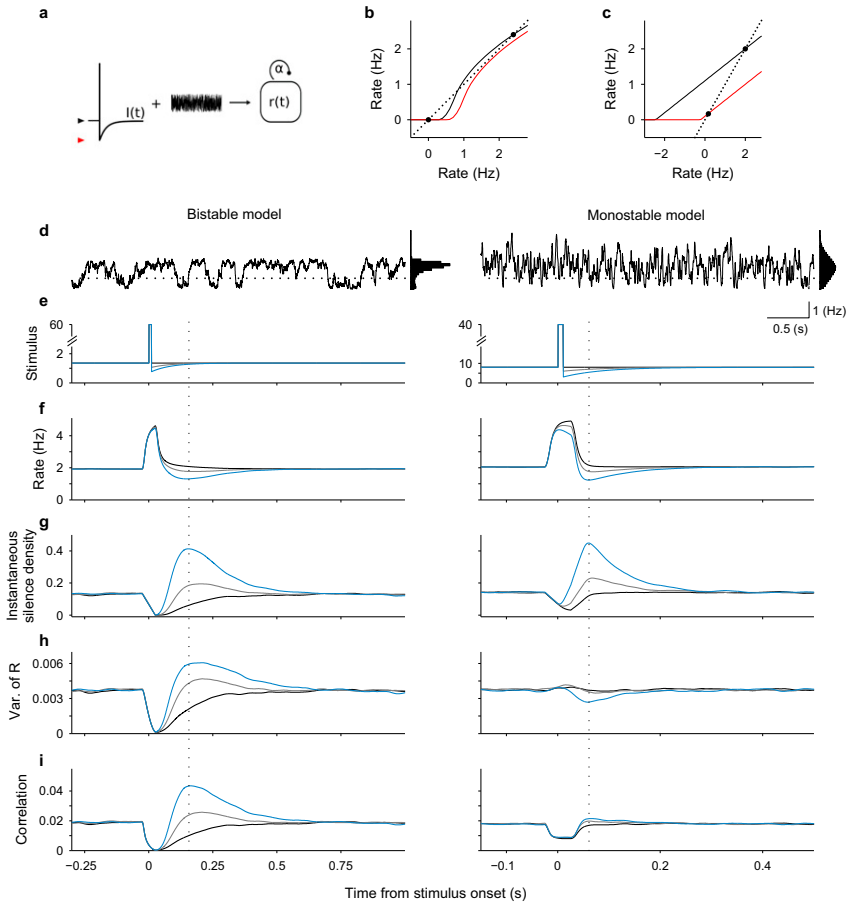

Fig. S9. Minimal model reproducing the key features of the stimulus-evoked dynamics of correlation. (*A*) Simplified network model with no adaptation composed of a recurrently coupled excitatory population receiving a fluctuating input $I(t)$ consisting of a brief stimulus (square pulse) and an after-stimulus suppression, mimicking the effect of short-term depression of the synaptic afferents. (*B* and *C*) Graphical representation of the stable fixed points of the system (filled circles) obtained from solving the equation: $r = \varphi(\alpha r + I - \theta)$. The identity line $r = x$ is shown as dotted. The transfer function $\varphi(\alpha r + I - \theta)$ (solid lines), shown for baseline I (black) and the suppressed I taken after stimulus offset (red; arrowheads in *A*), was sigmoidal for the bistable model (*B*) or linear-threshold in the monostable model (*C*). (*D*) Example rate traces during spontaneous activity (*Left*). For each model, the parameters were chosen to yield the same baseline values for mean rate, integrated rate variance R, and silent density S corresponding to the intermediate brain state (dotted line represents silence threshold at 1 Hz). The distribution of $r(t)$ is bimodal in the bistable model and approximately Gaussian in the monostable model (*Right*). (*E–I*) Stimulus (*E*), mean evoked instantaneous rate $r(t)$ (*F*), silence density $S(t)$ (*G*), variance of integrated rate $R(t)$ (*H*), and instantaneous correlation $\rho(t)$ (*I*) obtained for the bistable (left panels) and monostable model (right panels) for three stimuli with a different level of after-stimulus suppression (color code in *E*). Stimulus parameters were chosen for each model to produce the same peak response and after-stimulus rate suppression levels (*E* and *F*). Because the rate distribution of the bistable model becomes unimodal at the response peak (Fig. 4*E*, *ii*), $S(t)$, the integrated rate variance, and $\rho(t)$ all show a prominent drop for all stimuli (*G–I*, *Left*). The monostable model, in contrast, suffers an upward displacement of the rate distribution with no decrease in variance (*H*; *Right*) and shows a smaller drop of $\rho(t)$ (*I*; *Right*), purely caused by the increase in mean rate (Eq. **S29**). Only the bistable model showed a robust rebound in $\rho(t)$ in response to stimuli with after-stimulus suppression (*I*, gray and blue traces). The monostable model did not display a rebound in $\rho(t)$ because the dynamics of the rate variance were qualitatively different (*H*, *Right*). Vertical dotted lines mark the time of the peak of the $S(t)$ rebound. Notice the different time range shown in left and right panels. Bistable model parameters: $g = 0.6$ Hz, $\alpha = 2.25$ s, $\theta = 2$, $I = 1.36$, and $\sigma = 2.8$. Monostable model parameters: $\theta = 2$, $I = 7.5$, and $\sigma = 9$.

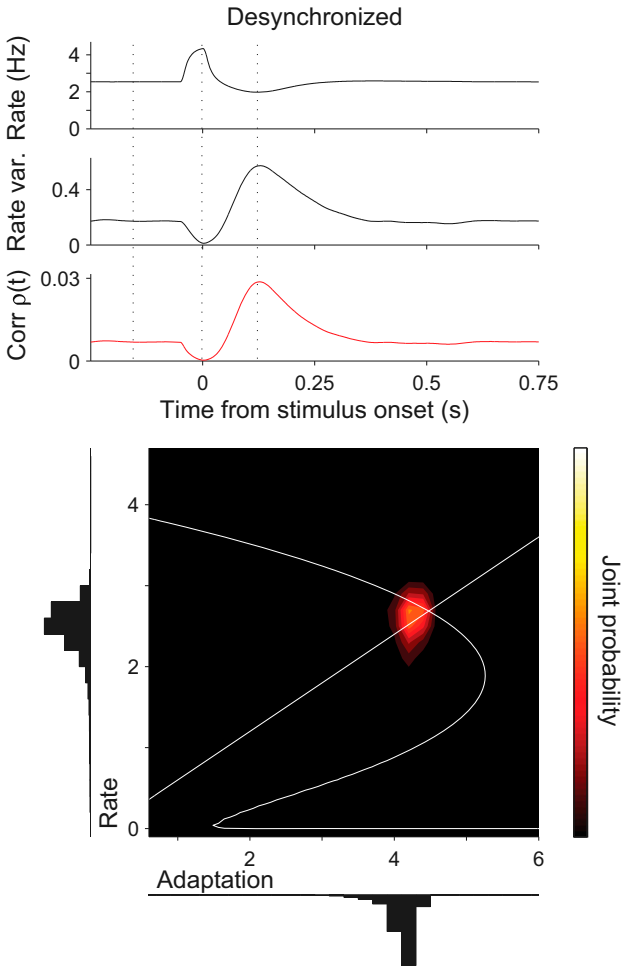

Movie S1. Rate model transient dynamics during the desynchronized brain state. From *Top* to *Bottom*: Stimulus-evoked mean instantaneous rate $r(t)$, rate variance, instantaneous correlation $\rho(t;T)$, and the instantaneous probability density of the system $P(r,a,t)$ given as a time-varying color map plotted on the (r,a) phase plane (hotter colors indicate larger probability). Rate and adaptation nullclines are superimposed (white cubic curve and straight line, respectively). Statistics were obtained across 10,000 repeated stimulus presentations. Time points *i–iii* discussed in the main text are marked with dotted lines. Marginal distributions $P(r,t)$ and $P(a,t)$ are plotted next to the rate and adaptation axes, respectively. Parameters were $I = 3.6$ and $\beta = 1.67$.

Movie S1

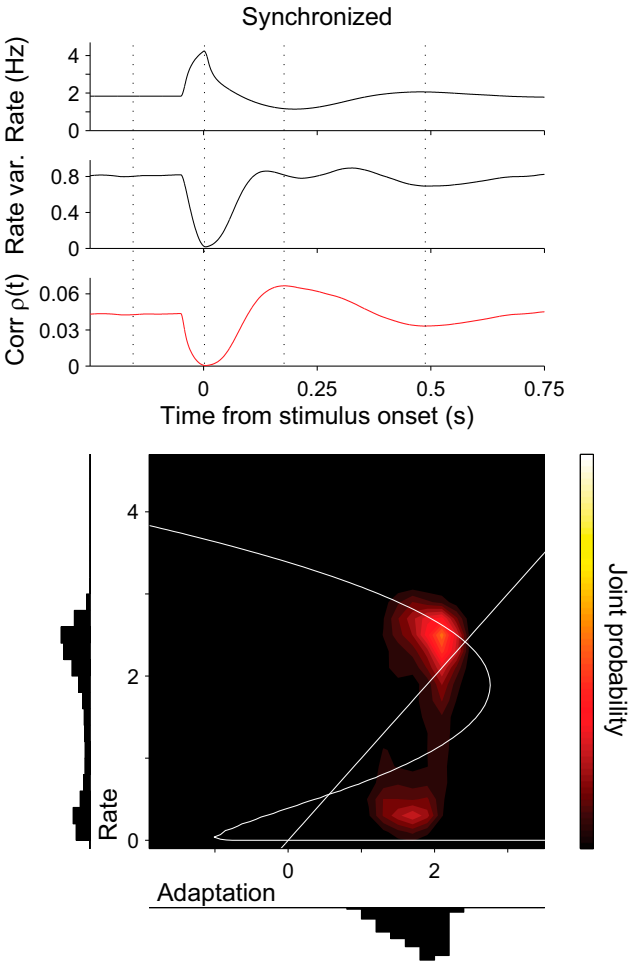

Movie S2. Rate model transient dynamics during the synchronized brain state. Convention as in Movie S1 except that the model was simulated with parameters $I = 1.1$ and $\beta = 1$ to exhibit the dynamics of the synchronized state.

Movie S2